Tsinidis, G. *et al.* (2015). *Géotechnique* **65**, No. 5, 401–417 [http://dx.doi.org/10.1680/geot.SIP.15.P.004]

Dynamic response of flexible square tunnels: centrifuge testing and validation of existing design methodologies

G. TSINIDIS*, K. PITILAKIS*, G. MADABHUSHI† and C. HERON†

A series of dynamic centrifuge tests were performed on a flexible aluminium square tunnel model embedded in Hostun dry sand. The tests were carried out at the centrifuge facility of the University of Cambridge in order to further improve knowledge regarding the seismic response of rectangular embedded structures and to calibrate currently available design methods. The soil–tunnel system response was recorded with an extensive instrumentation array, comprising miniature accelerometers, pressure cells and position sensors in addition to strain gauges, which recorded the tunnel lining internal forces. Tests were numerically analysed by means of full dynamic time history analysis of the coupled soil–tunnel system. Numerical predictions were compared to the experimental data to validate the effectiveness of the numerical modelling. The interpretation of both experimental and numerical results revealed, among other findings: (*a*) a rocking response of the model tunnel in addition to racking; (*b*) residual earth pressures on the tunnel side walls; and (*c*) residual internal forces after shaking, which are amplified with the tunnel's flexibility. Finally, the calibrated numerical models were used to validate the accuracy of simplified design methods used in engineering practice.

KEYWORDS: centrifuge modelling; earthquakes; numerical modelling; soil/structure interaction; tunnels & tunnelling

INTRODUCTION

Recent earthquake events have demonstrated that underground structures in soft soils may undergo extensive damage or even collapse (Dowding & Rozen, 1978; Sharma & Judd, 1991; Iida *et al.*, 1996; Kawashima, 2000; Wang *et al.*, 2001; Kontoe *et al.*, 2008). These failures increased interest in further investigation of the seismic response of these types of structures. Generally, the seismic response of embedded structures is quite distinct from that of above-ground structures, as the kinematic loading induced by the surrounding soil prevails over inertial loads stemming from the oscillation of the structure itself (Kawashima, 2000). In addition, large embedded structures are commonly stiff structures to withstand static loads. Hence, during earthquake shaking, strong interaction effects are mobilised between the structure and the surrounding soil, especially for structures of rectangular cross-section. These interaction effects are mainly affected by two crucial parameters, namely: (*a*) the soil to structure relative flexibility and (*b*) the soil–structure interface characteristics. In general, both are changing with the amplitude of seismic excitation, as they depend on the soil shear modulus and strength, which are related to the ground strains and the non-linear behaviour of the soil.

Several methods are available in the literature for the evaluation of the response of underground structures and tunnels under seismic shaking (e.g. St John & Zahrah, 1987; Wang, 1993; Penzien, 2000; AFPS/AFTES, 2001; Hashash *et al.*, 2001; ISO, 2005; Anderson *et al.*, 2008; FHWA, 2009). The results of these methods may deviate, even under the same design assumptions, especially in case of rectangular structures (e.g. cut and cover tunnels), owing to both inherent epistemic uncertainties and a knowledge shortfall regarding some crucial issues that significantly affect the seismic response (Pitilakis & Tsinidis, 2014). Seismic earth pressures and shear stresses distributions along the perimeter of the embedded structure and complex deformation modes during shaking for rectangular cross–sections (e.g. rocking and inward deformations) are, among other issues, still not entirely understood.

The knowledge shortfall motivated a range of experimental (e.g. Chou *et al.*, 2010; Shibayama *et al.*, 2010; Chian & Madabhushi, 2012; Cilingir & Madabhushi, 2011a, 2011b, 2011c; Lanzano *et al.*, 2012; Chen *et al.*, 2013), numerical (e.g. Anastasopoulos *et al.*, 2007, 2008; Amorosi & Boldini, 2009; Anastasopoulos & Gazetas, 2010; Kontoe *et al.*, 2011; Lanzano *et al.*, 2014) and analytical (e.g. Huo *et al.*, 2006; Bobet *et al.*, 2008; Bobet, 2010) research studies over recent years, investigating the effects of seismic shaking and earthquake-induced ground failures (e.g. liquefaction) on the response of embedded structures. In some cases, the efficiency of different design methods has been investigated by comparing the outcomes of the methods (e.g. tunnel distortions or dynamic internal forces) with each other (e.g. Hashash *et al.*, 2005, 2010; Kontoe *et al.*, 2014).

This study presents a series of dynamic centrifuge tests that were performed on a flexible aluminium square tunnel model embedded in dry sand. The soil–tunnel system response was recorded with an extensive instrumentation array comprising miniature accelerometers, pressure cells and position sensors, in addition to strain gauges, which recorded the tunnel lining internal forces. The test case is also numerically analysed by means of a full dynamic time history numerical analysis of the coupled soil–tunnel system. Numerical predictions are compared to the experimental data to validate the effectiveness of the numerical modelling. The calibrated numerical models are finally used to validate the accuracy of available simplified design methods used in engineering practice.

DYNAMIC CENTRIFUGE TESTING

The test was carried out on the 10 m diameter Turner beam centrifuge of the University of Cambridge (Schofield,

Manuscript received 31 March 2014; revised manuscript accepted 23 December 2014. Published online ahead of print 20 March 2015.
Discussion on this paper closes on 1 October 2015, for further details see p. ii.
* Department of Civil Engineering, Aristotle University, Thessaloniki, Greece.
† Schofield Centre, University of Cambridge, Cambridge, UK.

1980) under a centrifuge acceleration of 50$\mathbf{g}$ (scale factor $n = 50$). A large equivalent-shear-beam (ESB) container was used to contain the model (Zeng & Schofield, 1996). Scaling laws that are applied to convert the measured quantities from model to prototype scale are summarised in Table 1 (Schofield, 1981).

The soil deposit was made of uniform Hostun HN31 sand with 90% relative density. The physical and mechanical properties of the sand are summarised in Table 2. Sand pouring was performed in layers using an automatic hopper system (Madabhushi *et al.*, 2006), while the model tunnel and the instruments were properly positioned during construction.

The model tunnel, manufactured using 6063A aluminium alloy, was 100 mm wide and 220 mm long, having a lining thickness of 2 mm (Fig. 1(a)). The aluminium alloy mechanical properties are summarised in Table 3. According to the scale factor, the model corresponds to a 5×5 (m) square tunnel having an equivalent concrete lining thickness equal to 0·13 m (assuming $E_c = 30$ GPa for the concrete). This thickness is obviously unrealistic in practice, as the design analysis for the static loads will result in a much thicker lining. However, this selection was made in order to study the effect of high flexibility on the tunnel response, as well as to obtain clear measurements of the lining bending and axial strains. To simulate more realistically the soil–tunnel interface, sand was stuck on the external face of the model tunnel, creating a rough surface. Two polytetrafluoroethylene (PTFE) rectangular plates were placed at each end of the tunnel to avoid the entry of sand into the tunnel. The plates, which were marginally larger than the model tunnel, were connected to each other by a rod which passed through the tunnel (Fig. 1(b)).

Table 1. Centrifuge scaling laws (Schofield, 1981)

Parameter	Model/Prototype	Dimensions
Length	$1/n$	l
Mass	$1/n^3$	m
Stress	1	$ml^{-1}t^{-2}$
Strain	1	1
Force	$1/n^2$	mlt^{-2}
Time (dynamic)	$1/n$	t
Frequency	n	t^{-1}
Acceleration	n	lt^{-2}
Velocity	1	lt^{-1}

Table 2. Hostun HN31 physical and mechanical properties

ρ_s: g/cm^3	e_{max}	e_{min}	d_{10}: mm	d_{50}: mm	d_{60}: mm	ϕ_{cv}: degrees
2·65	1·01	0·555	0·209	0·335	0·365	33

Table 3. Model tunnel mechanical properties

Unit weight, γ_t: kN/m^3	Young's modulus, E: GPa	Poisson ratio, υ	Tensile strength, f_{bk}: MPa
2·7	69·5	0·33	220

A dense instrumentation array was implemented to monitor the soil–tunnel response (Fig. 2). Miniature piezoelectric accelerometers were used to measure the acceleration in the soil, on the tunnel and on the container. The soil surface settlements were recorded in two locations using linear variable differential transformers (LVDTs), while two position sensors (POTs) were attached to the upper edges of the tunnel walls to capture the vertical displacement and the possible rocking of the model tunnel. Both the LVDTs and the POTs were attached to gantries running above the ESB container. Two miniature total earth pressure cells (PCs) were attached to the left side wall of the tunnel, allowing the measurement of the soil earth pressures on the wall. Strain gauges were attached to the inner and outer faces of the tunnel to measure the lining bending moment and axial force at several locations (Fig. 2). Unfortunately, the bending moment strain gauge at the middle of the roof slab (SG-B3) malfunctioned during testing. All the instruments were properly calibrated before and checked after testing. The strain gauges were carefully calibrated for static loading patterns using the procedure outlined in Tsinidis *et al.* (2014a). The data were recorded at a sampling frequency of 4 Hz during the swing up of the centrifuge and at 4 kHz during shaking.

A series of air hammer tests was performed to estimate the soil shear wave velocity profile (Ghosh & Madabhushi, 2002). A small air hammer was introduced close to the base of the soil layer, while a set of accelerometers (AH, Fig. 2) were placed above it, forming a vertical array, allowing a record of the arrival times of the waves emanating from the air hammer. To ensure that the arrival times were adequately recorded, the accelerometers along this array were attached to a different acquisition system that allowed for a sampling frequency of 50 kHz.

The dynamic input was provided at the container base by a stored angular momentum actuator, designed to apply

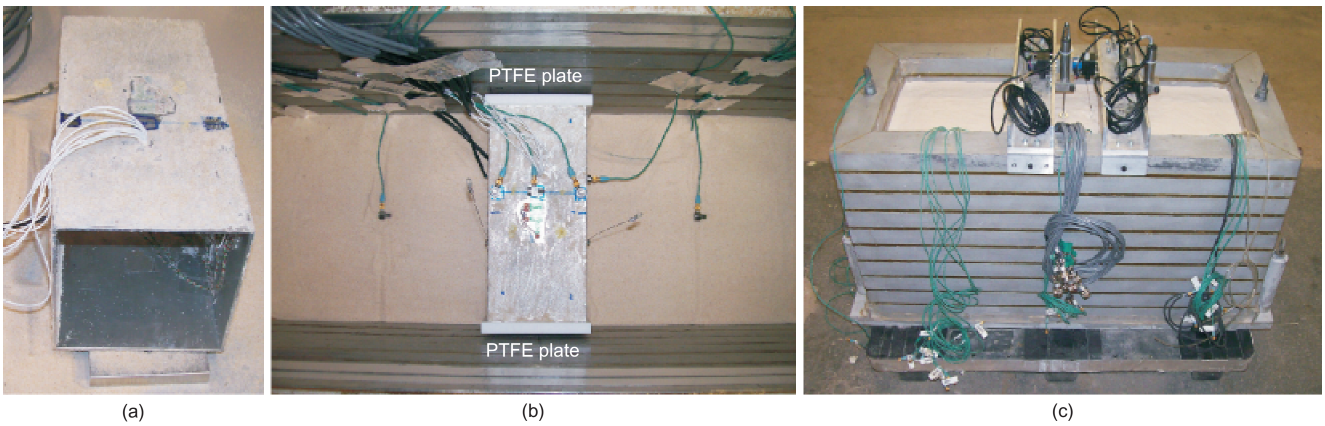

Fig. 1. (a) Model tunnel; (b) model tunnel placement in the equivalent shear beam container; (c) completed model in the equivalent shear beam container

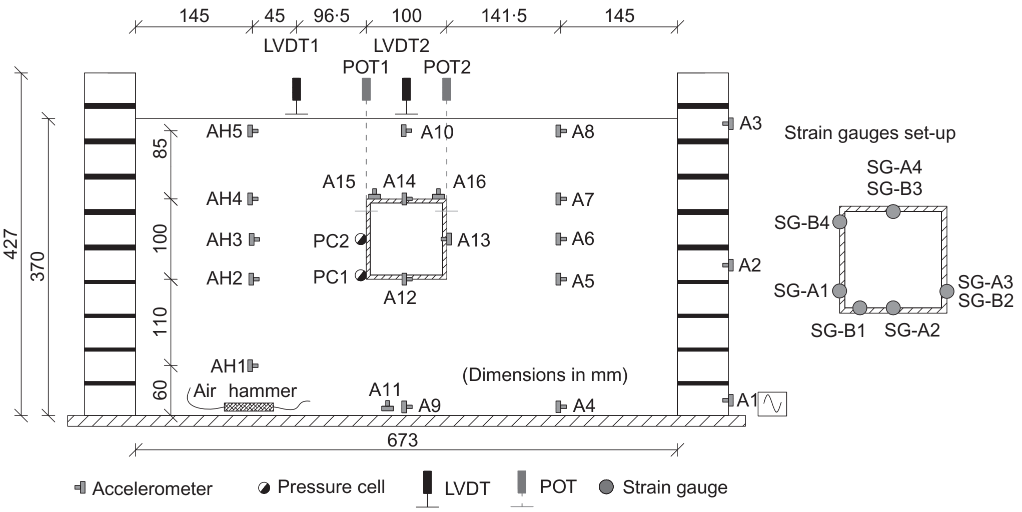

Fig. 2. Model layout and instrumentation scheme (A: accelerometer; AH: accelerometer above air hammer; LVDT: linear variable differential transformer; POT: position sensor; SG-A: axial strain gauge; SG-B: bending moment strain gauge; PC: pressure cell)

sinusoidal or sine-sweep wavelets (Madabhushi *et al.*, 1998). The model was subjected to a total of eight earthquakes during two flights: EQ1 to EQ5 were fired during a first flight, whereas EQ6 to EQ8 were fired during a subsequent flight. Fig. 3 presents the input motion–time histories, while Table 4 tabulates their characteristics. During each flight, the centrifuge was spun up in steps until 50***g*** and then the earthquakes were fired in a row, leaving some time between them to acquire the data.

To interpret the experimental results, the data were windowed, neglecting the parts of the signals before and after the main shake duration, while a filtering procedure was conducted in the frequency domain. In particular, acceleration–time histories were filtered at 10 to 400 Hz using a band pass eighth-order Butterworth filter. All the other data were filtered using a low-pass eighth-order Butterworth filter at 400 Hz.

NUMERICAL ANALYSIS

Numerical model

The test was numerically simulated by means of full dynamic time history analyses, using the finite-element code Abaqus (Abaqus, 2012). The analyses were performed in

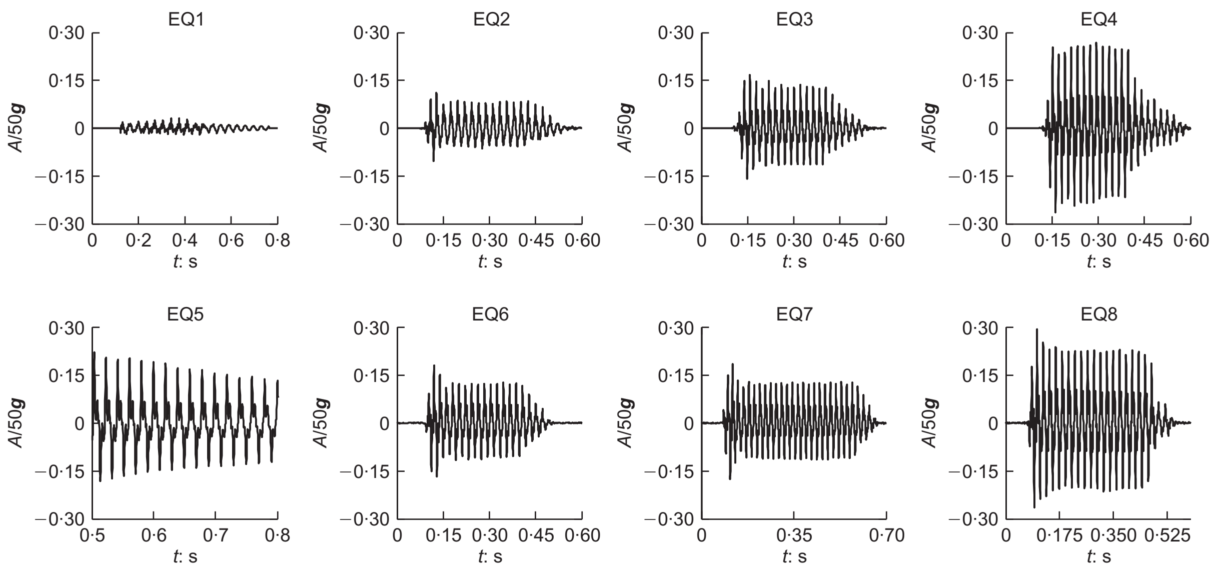

Fig. 3. Input motion–time histories

Table 4. Input motions characteristics (bracketed values in prototype scale)

EQ ID	EQ1	EQ2	EQ3	EQ4	EQ5*	EQ6†	EQ7†	EQ8†
Frequency, *f*: Hz	30 (0·6)	45 (0·9)	50 (1)	50 (1)	60 (1·2)	50 (1)	50 (1)	50 (1)
Amplitude, *a*: ***g***	1·0 (0·02)	4·0 (0·08)	6·5 (0·13)	12·0 (0·24)	12·0 (0·24)	5·8 (0·116)	6·0 (0·12)	11·0 (0·22)

* Sine sweep.
† Fired during a second flight.

prototype scale assuming plane strain conditions. Fig. 4 presents the numerical model layout.

The soil was meshed with quadratic plane strain elements, while the tunnel was simulated with beam elements. The element size was selected in a way that ensured efficient reproduction of the waveforms of the whole frequency range under study.

The base boundary of the model was simulated as rigid bedrock (shaking table), while for the side boundaries kinematic tie constraints were introduced, forcing the opposite vertical sides to move simultaneously, simulating, in that simplified way, the container.

The soil–tunnel interface was modelled using a finite sliding hard contact algorithm embedded in Abaqus (Abaqus, 2012). The model constrains the two media when attached, using the penalty constraint enforcement method and Lagrange multipliers, while it also allows for separation. The interface friction effect on the soil–tunnel system response was investigated by applying different Coulomb friction coefficients μ, namely $\mu = 0$ for the full slip and 0·4 and 0·8 for non-slip conditions. In a final series of analyses, the soil and the tunnel were fully bonded, assuming no slip conditions, precluding separation.

The model tunnel was modelled using an elastic–perfectly plastic material model, with yield strength equal to 220 MPa, while the soil response under seismic shaking was simulated in two ways. In a first series of analyses, a visco-elastic model was implemented, introducing a degraded shear modulus distribution and viscous damping (e.g. following the equivalent linear approximation method). In the second series of analyses, a non-associated Mohr–Coulomb model was used to account for the permanent deformations of the soil. The latter model, embedded in Abaqus, allows for simulation of certain hardening or softening responses after yielding. Elastic properties were assumed the same with the visco-elastic analyses, following a similar procedure as in Amorosi & Boldini (2009). This elasto-plastic model has been implemented by several researchers (e.g. Pakbaz & Yareevand, 2005; Hwang & Lu, 2007), while it has been recently used by Cilingir & Madabhushi (2011a, 2011b, 2011c) for the simulation of similar dynamic centrifuge tests on model tunnels in dry sand, revealing reasonable comparisons between the recorded data and the numerical results. The implemented models were selected as they are proposed in guidelines for dynamic analysis of embedded structures (e.g. equivalent linear approximation in FHWA (2009)) and are commonly used in tunnelling design practice owing to their easy calibration and control. Recently, a series of dynamic centrifuge tests on a flexible circular model tunnel embedded in dry sand (Lanzano *et al.*, 2012) has been used as a benchmark of a numerical round robin on tunnel tests (Bilotta *et al.*, 2014). Several research groups have simulated the tests using different numerical codes and constitutive models of different complexity (Amorosi *et al.*, 2014; Conti *et al.*, 2014; Gomes, 2014; Hleibieh *et al.*, 2014; Tsinidis *et al.*, 2014b). Among the most interesting results of this comparative effort is that even sophisticated constitutive models produced results that deviated considerably from the recorded data. Part of the difference was attributed to calibration issues and determination of constitutive parameters.

The input motion was introduced at the model base in terms of acceleration–time histories, referring to the motion recorded by the reference accelerometer (A1, Fig. 2). The analyses were performed in two steps: first the gravity loads were introduced, while in a second step the earthquake motions were applied in a row, replicating each test flight. To this end, the loading history for the sand was accounted for.

Sand stiffness and strength

The sand small-strain shear modulus (G_{max}) was described according to Hardin & Drnevich (1972), which fits reasonably well with the air hammer test results and also results of laboratory tests (resonant column) that were performed on the specific sand fraction (Pistolas *et al.*, 2014). Fig. 5 compares the estimated small-strain shear wave velocity gradient from different methods and the distribution proposed according to Hardin & Drnevich (1972). It is worth noting that these results refer to the 'free-field' conditions away from the model tunnel. The exact properties of sand in the area close to the tunnel are not well known. The reason is that considering the model's formation (i.e. sand pouring from a height to achieve the desired relative density of the soil specimen), the existence of the model tunnel may affect the density of the sand in the adjacent zone, thus affecting the mechanical properties of the sand at this location. However, it is believed that after the first shakes the soil in this particular region will have reached a reasonable degree of densification comparable to the rest of the soil sample.

To estimate the real sand stiffness and viscous damping during shaking a trial-and-error procedure was applied. More specifically, one-dimensional (1D) equivalent linear (EQL) soil response analyses of the soil deposit were performed, using different sets of G–γ–D curves for cohesionless soils (e.g. Seed *et al.*, 1986; Ishibashi & Zhang, 1993; Pistolas *et al.*, 2014). The analyses were performed in the frequency domain using EERA (equivalent-linear earthquake site response analyses) (Bardet *et al.*, 2000). The computed

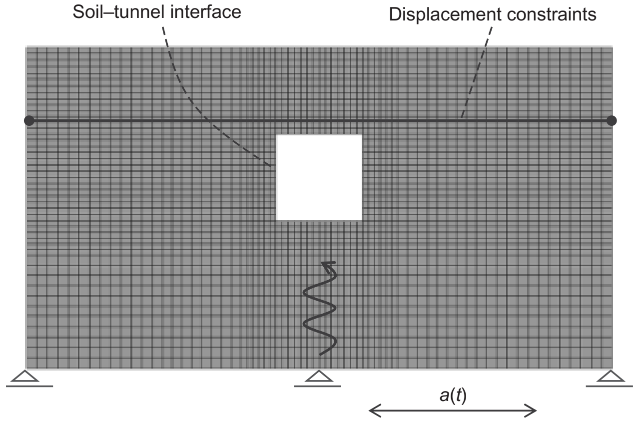

Fig. 4. Numerical model in Abaqus

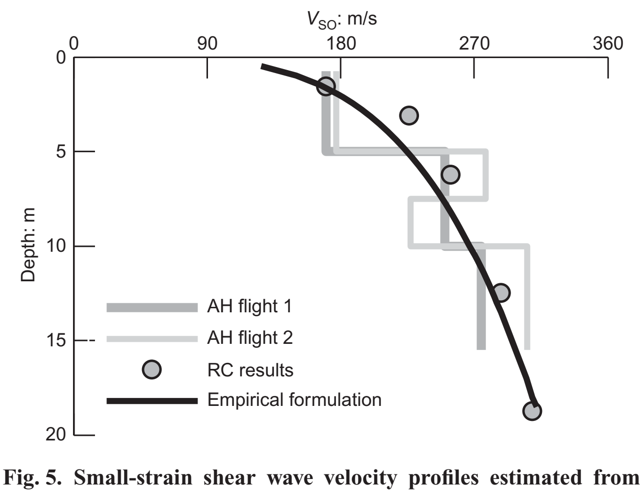

Fig. 5. Small-strain shear wave velocity profiles estimated from air hammer tests (AH) and resonant column tests (RC) compared to the Hardin & Drnevich (1972) empirical formulation

horizontal acceleration–time histories and amplification were compared to the recorded data of the free field array (sensors A4 to A8 in Fig. 2). The adopted G–γ–D curves were those that resulted in the best fitting of the numerical predictions with the experimental results (Ishibashi & Zhang (1993) for small confining pressure). Comparisons of the adopted G–γ–D curves with empirical ones (Seed *et al.*, 1986) and laboratory results from resonant column and cyclic triaxial tests for the specific sand fraction (Pistolas *et al.*, 2014) are provided in Fig. 6. The adopted numerical curves compare reasonably well with the laboratory test results over a wide range of strain amplitudes.

One-dimensional equivalent linear soil response analyses for the finally selected G_{max} and G–γ–D curves revealed that a reduced Hardin and Drnevich distribution adequately reproduced the degraded sand shear modulus during shaking. To this end, the following expression was used for the description of the degraded strain shear modulus

$$G = \alpha \times 100 \frac{(3-e)^2}{1+e}(\sigma')^{0\cdot 5} \tag{1}$$

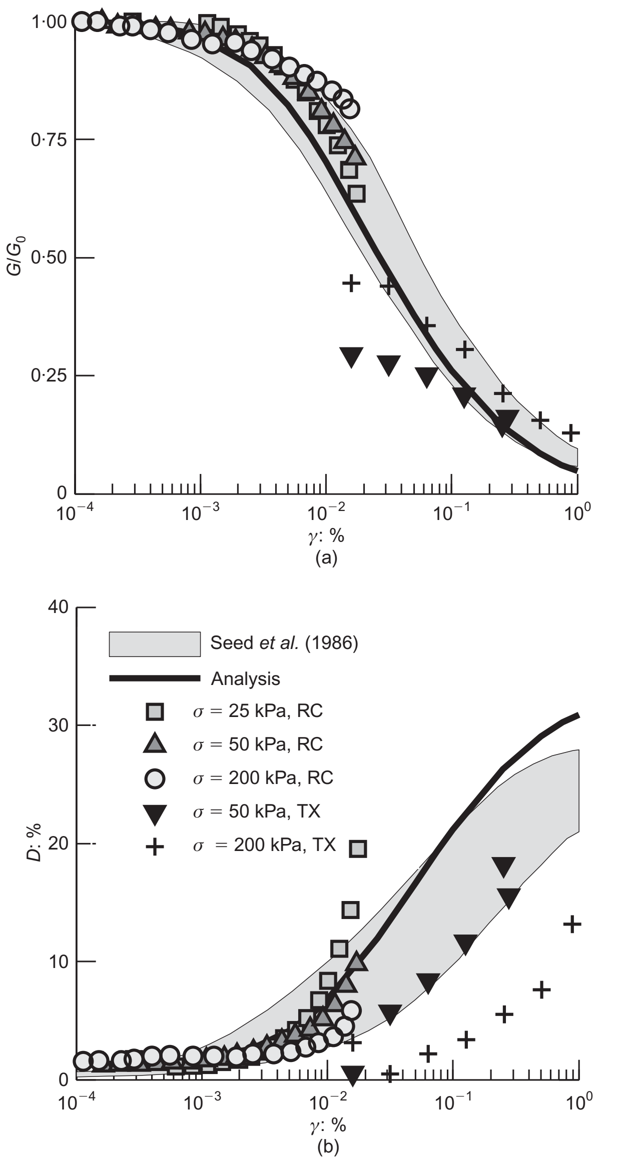

Fig. 6. Adopted *G*–*γ*–*D* curves compared to resonant column test results (RC) (Pistolas *et al.*, 2014), cyclic triaxial test results (TX) (Pistolas *et al.*, 2014) and empirical proposals (Seed *et al.*, 1986): (a) *G*/*G*$_0$ plotted against shear strain; (b) damping plotted against shear strain

where e is the void ratio, σ' is the mean effective stress (in MPa), G is the degraded shear modulus (in MPa) and α is the reduction value for each shake, ranging between 0·3 and 0·4. For the computation of the mean effective stress the earth coefficient at rest (K_0) was evaluated as (Jaky, 1948)

$$K_0 = 1 - \sin\phi \tag{2}$$

where ϕ is the sand friction angle.

The reduced values for the sand shear modulus come in agreement with the shear moduli computed from the stress–strain loops, estimated using the recorded acceleration–time histories across the free-field array (A4–A8 in Fig. 2), following Zeghal & Elgamal (1994). It is noteworthy that this high decrease of the soil stiffness and increase of damping in this type of test is also reported by other researchers (Kirtas *et al.*, 2009; Pitilakis & Clouteau, 2010; Lanzano *et al.*, 2010, 2014; Li *et al.*, 2013).

In the final two-dimensional (2D) full dynamic analysis, the degraded elastic stiffness of the sand material for each shake was introduced through a Fortran user subroutine, which correlates the stiffness with the confining pressure at each soil element integration point. To this end, the effect of the tunnel on the surrounding sand stiffness was explicitly accounted for.

In both visco-elastic and visco-elasto-plastic analyses, viscous damping was introduced in the form of the frequency dependent Rayleigh type. 'Target' damping (15%) was estimated through the 1D equivalent linear response analyses, as discussed before. For the calibration of the Rayleigh parameters, the double frequency approach was implemented. The Rayleigh parameters were properly tuned for different 'important frequencies' (e.g. soil deposit dominant frequencies or signal dominant frequencies). The finally selected parameters were those that resulted in good comparisons between the computed and recorded acceleration data. The importance of proper calibration for the Rayleigh coefficients is discussed in Kontoe *et al.* (2011). In the elasto-plastic analyses, additional energy dissipation was introduced by the hysteretic soil response.

Regarding the strength parameters of the sand, a friction angle ϕ equal to 33° (critical friction angle for the specific sand fraction) was used, while the dilatancy angle ψ was assumed equal to 3° (Schanz & Vermeer, 1996). These strength parameters correspond to the specific sand fraction and are found to give reasonable comparisons with the recorded response. A slight cohesion ($c = 1$ kPa) was introduced to avoid numerical problems.

NUMERICAL PREDICTIONS COMPARED WITH EXPERIMENTAL RESULTS

Representative comparisons between the recorded and the computed response are presented in this section. Through the presentation of relevant data several crucial aspects of the soil–tunnel response are discussed. Results are generally shown at model scale, if not stated otherwise.

Horizontal acceleration

Figure 7 presents time windows of typical comparisons between the recorded and the computed acceleration–time histories at two representative locations (middle section of left side wall, A13; top receiver of tunnel accelerometer array, A10). In Fig. 8 representative comparisons between the computed and recorded horizontal acceleration amplification along the free-field and the tunnel vertical accelerometer arrays are depicted. Generally, both visco-elastic and elasto-plastic analyses reveal similar responses and amplification, while numerical predictions are in good agreement with the

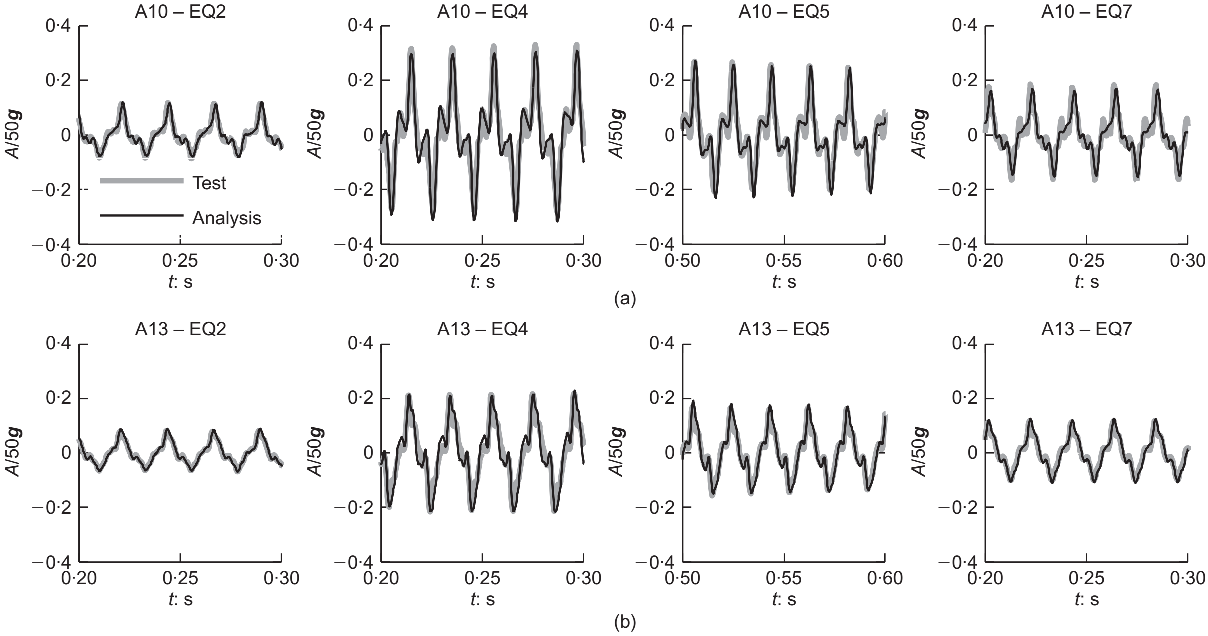

Fig. 7. Time windows of representative acceleration–time histories recorded and computed for different earthquake input motions; experimental data compared with visco-elasto-plastic results: (a) accelerometer A10 at the soil surface above the model tunnel; (b) accelerometer A13 on the tunnel side-wall (notation according to Fig. 2)

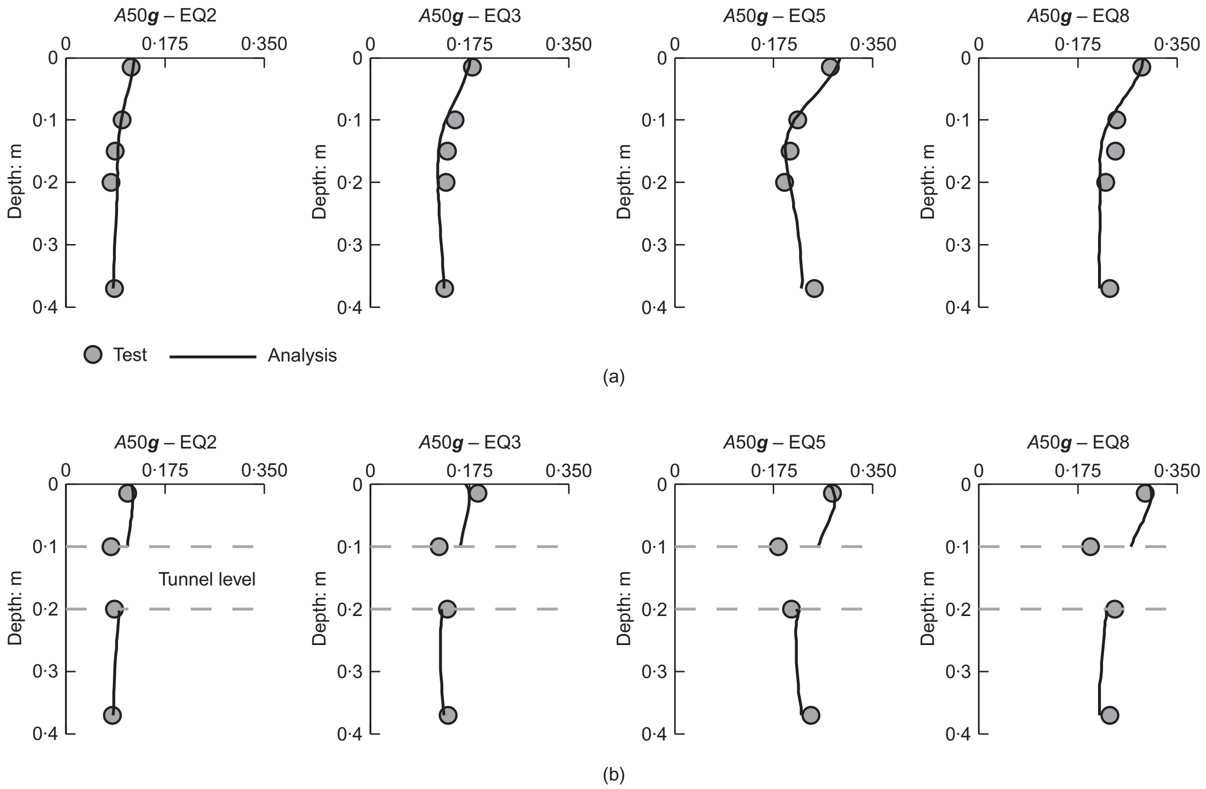

Fig. 8. Horizontal acceleration amplification along (a) the soil free-field accelerometers vertical array, and (b) the tunnel accelerometers vertical array, for different earthquake input motions; experimental data compared with visco-elasto-plastic results

records both in terms of amplitude and frequency content (Fig. 9). The differences, generally minor, are attributed to the inevitable differences between the assumed soil mechanical properties (stiffness and damping) and their actual values during the test, especially near the tunnel. The larger deviation observed at the tunnel roof slab is attributed to an erroneous record at this location. Actually, the slab inward deformations, discussed in the following section, are likely to have caused a malfunction of the accelerometer at this location. It worth mentioning the higher frequencies of the signals observed in the Fourier spectra shown in Fig. 9. Significant energy content is associated with higher frequencies than with the predominant one. These higher frequencies, which are attributed to the experimental equipment's

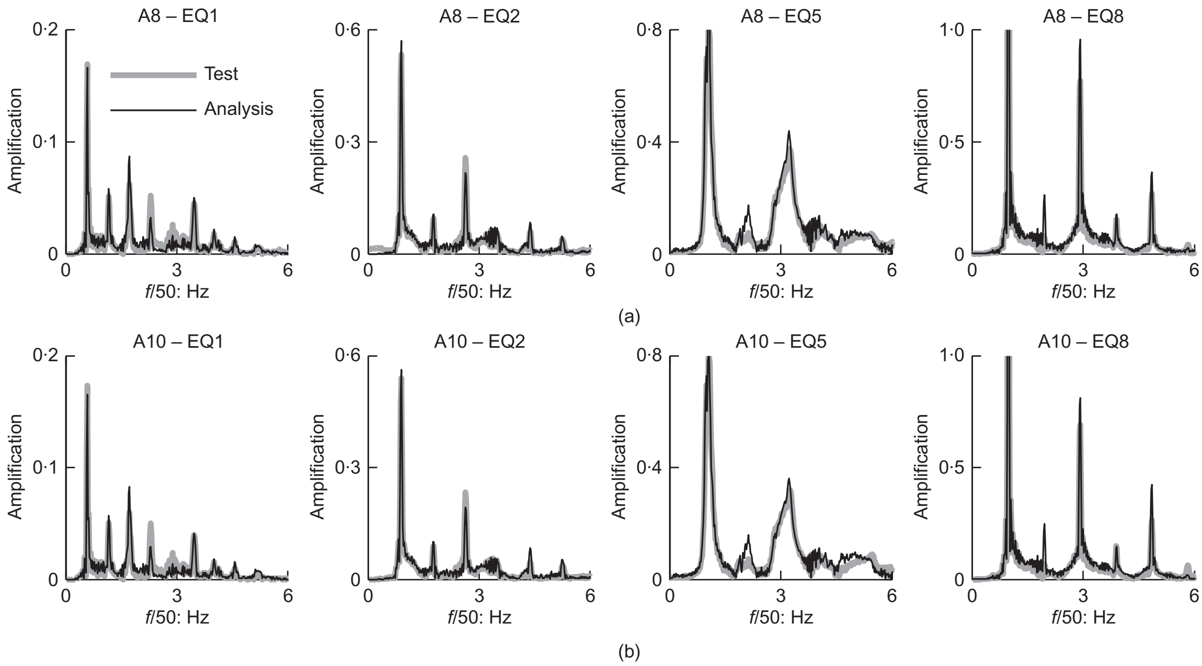

Fig. 9. Fourier spectra of acceleration–time histories recorded and computed at locations of (a) accelerometer A8 and (b) accelerometer A10 for different earthquake input motions; experimental data compared with visco-elasto-plastic results

mechanical response (Brennan *et al.*, 2005), are described quite efficiently by the numerical model.

Tunnel deformed shapes

Figure 10 presents time windows of typical comparisons between the recorded and computed vertical accelerations at the sides of the tunnel roof slab. Experimental results are slightly larger than the numerical predictions. The difference is attributed to the parasitic yawing movement of the whole model on the shaking table during shaking, which may amplify vertical acceleration and cannot be reproduced by the numerical analysis. The no-slip condition analysis results are closer to the recorded response. Generally, signals are out of phase, indicating a rocking mode of vibration for the tunnel, in addition to the racking mode. Fig. 11 presents typical computed deformed shapes of the tunnel during shaking, verifying this complex racking–rocking response. Owing to the high flexibility of the tunnel, inward deformations are also observed for the slabs and the walls.

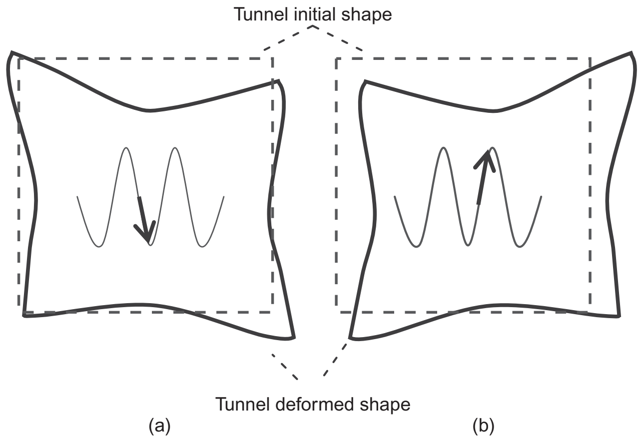

Fig. 11. Shape of deformed tunnel for time steps of the computed maximum racking distortion; EQ4 earthquake, elasto-plastic analysis for no slip conditions: (a) motion towards left; (b) motion towards right (deformations scale ×60)

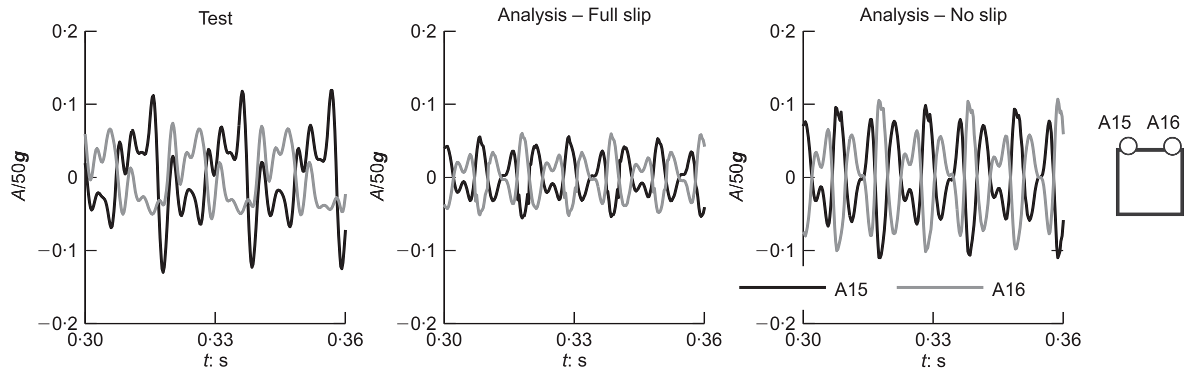

Fig. 10. Time windows of recorded and computed vertical acceleration–time histories at the sides of the tunnel roof slab for EQ4 earthquake; experimental data compared with visco-elasto-plastic results

Dynamic earth pressures

Typical comparisons between the computed and recorded dynamic earth pressures–time histories at the left side wall are presented in Fig. 12. The effect of the soil–tunnel interface characteristics on the computed earth pressures is also highlighted. Residual values are presented in records after shaking as a result of the soil yielding and densification around the tunnel. This post-earthquake residual response has also been reported during similar centrifuge tests (Cilingir & Madabhushi, 2011a, 2011b) and is amplified with the flexibility of the tunnel. In addition, dynamic pressure increments are found to be larger near the stiff corners of the tunnel. Generally, numerical predictions for no-slip conditions are closer to the recorded response. The comparison is more satisfactory, especially for the last shakes. Observed differences in amplitude can be attributed to the discrepancies between the assumed and the actual in test mechanical properties of the sand and the soil–tunnel interface, the efficiency of the constitutive models, and also to recording issues that are related to the response of the miniature earth pressures cells in the case of granular dry sands. Accurate measurement of earth pressures in sands with miniature pressure cells is always difficult, as the relative stiffness of the sensing plate may affect the readings, while there are also problems related to the grain size effect (Cilingir, 2009). Moreover, inward deformations of the tunnel wall may slightly change the recording direction (small inclination of the pressure cell) and therefore the recorded earth pressure may be different from the 'normal' value computed by the analysis. Considering the aforementioned points, the comparisons indicate a reasonable agreement.

Figure 13 presents typical dynamic earth pressure distributions around the tunnel's perimeter, referring to the time step of the tunnel maximum racking distortion. Soil yielding around the tunnel results in stress redistributions leading to a slightly different response between elasto-plastic and visco-

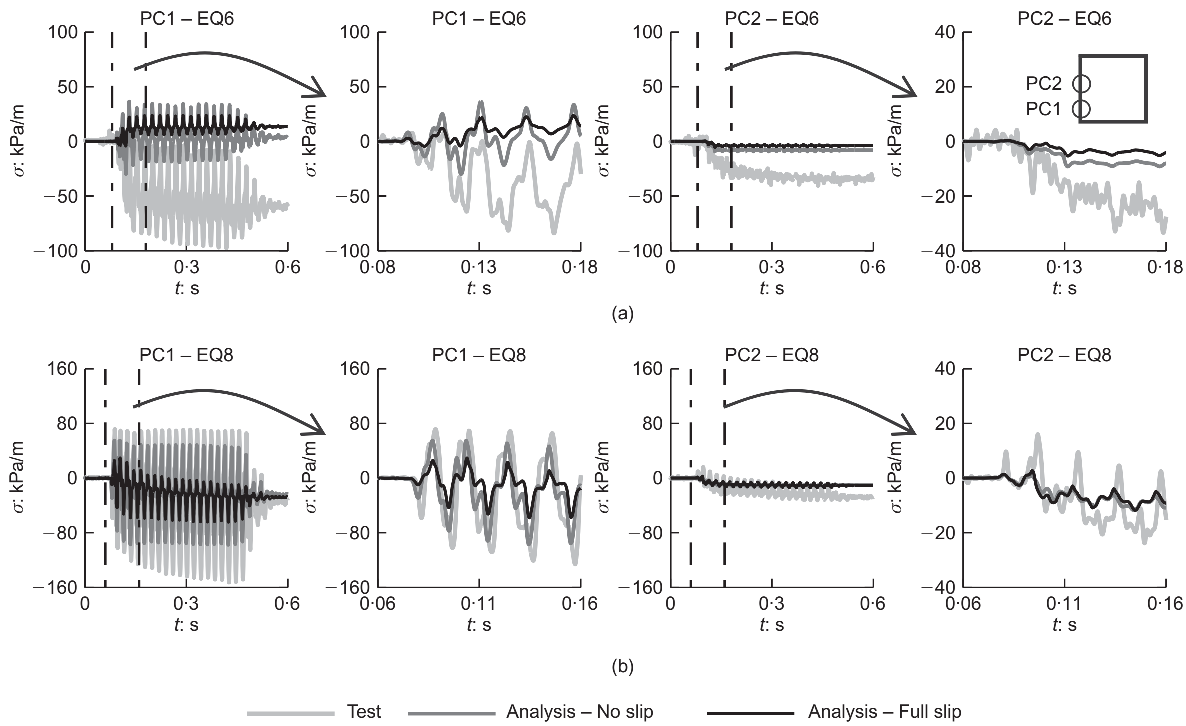

Fig. 12. Dynamic earth pressure–time histories recorded and computed by visco-elasto-plastic analyses on the left side wall for different earthquake input motions; effect of the soil–tunnel interface characteristics: (a) earthquake EQ6; (b) earthquake EQ8

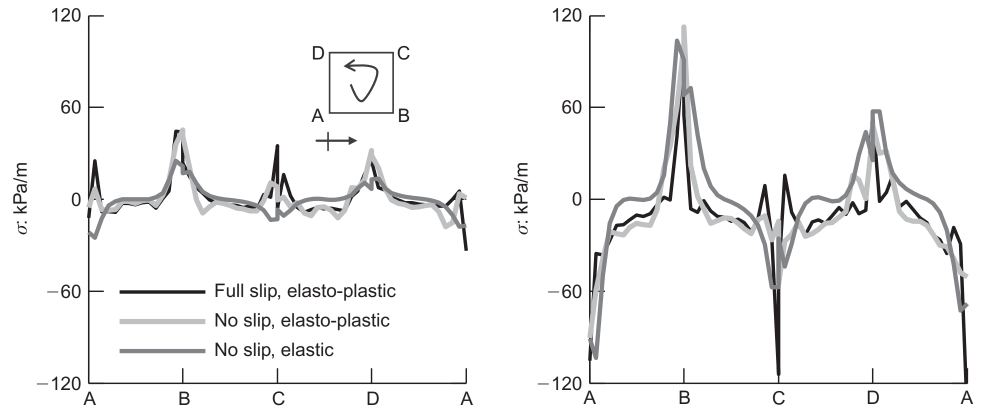

Fig. 13. Effect of soil–tunnel interface characteristics and soil yielding response on the dynamic earth pressures distributions computed along the perimeter of the tunnel at the time step of maximum racking distortion: (a) earthquake EQ2; (b) earthquake EQ4

elastic analyses (effect on distributions). Moreover, soil–tunnel interface properties seem to affect the soil yielding response in the area adjacent to the tunnel (Fig. 14) and therefore the pressure distributions. This relation between the soil yielding response and the soil–tunnel interface properties is also reported by Huo *et al.* (2005).

Soil dynamic shear stresses

Figure 15 portrays representative soil dynamic shear stress distributions around the tunnel computed for the time step of maximum racking distortion. As for the earth pressures, soil yielding affects the soil shear stress around the tunnel. Generally, shear stresses tend to increase near the tunnel corners due to the higher earth pressures (confining pressures for the tunnel) at these locations. As expected, interface friction plays an important role on the shear stress distribution and magnitude. An increase of the soil–tunnel interface friction results in an increase of the soil shear stresses along the middle sections of the tunnel slabs and walls.

Lining dynamic bending moment

Representative comparisons between recorded and computed by elasto-plastic analyses dynamic bending moment–time histories are presented in Fig. 16. Both experimental data and numerical predictions indicate a post-earthquake residual response, similar to that of the earth pressures. This residual response is highly affected by the tunnel's flexibility. Different assumptions for the soil–tunnel interface characteristics may affect the computed bending moments both in terms of residuals and dynamic increments, mainly due to the different soil yielding response around the tunnel in each case. Fig. 17 illustrates this effect on the residual bending moments computed for different shaking scenarios. It is noteworthy that the recorded residual bending moments for EQ7 are much lower than EQ6, although both input motions share the same amplitude and frequency characteristics. This is attributed to the fact that the largest part of soil plastic strain that is induced by the specific input motion amplitude (the same for both shakes) is accumulated during the first loading circles of the first shake (EQ6). This phenomenon is simulated reasonably well by the implemented elasto-plastic model.

Lining dynamic axial force

Similar to the dynamic bending moments, residual values were recorded for the lining axial forces (Fig. 18). Residuals were generally smaller than the ones of the bending moment, but were larger along the slabs. In addition, dynamic axial forces recorded on the side walls were out of phase, verifying the racking–rocking response of the tunnel during shaking (Tsinidis *et al.*, 2014a). Numerical results revealed similar tendencies. The effect of the mobilised friction (along the interface) on the lining axial forces is quite important (Fig. 18). Similar to the dynamic earth pressures, recorded axial forces were found to be in better agreement with the numerical predictions assuming no-slip conditions. This observation may be attributed to the inward deformations of the model tunnel that are amplified by the tunnel's high flexibility. The surrounding sand is actually squeezing the tunnel, leading to a more rigid soil–tunnel interface (no separation–no-slip conditions).

Generally, both the visco-elastic and the elasto-plastic analyses reproduce the recorded dynamic internal forces increments (reversible component of force increments) reasonably well (Fig. 19). These increments, which are computed as the half of the amplitude of the maximum values of the loading cycles in the internal forces–time histories, are in both cases amplified near the tunnel corners (Fig. 19).

SIMPLIFIED ANALYSIS METHODS

Simplified methods are commonly used in design practice, especially during preliminary stages of design, mainly due to their simplicity and reduced computational cost compared to the non-linear full dynamic analysis. The majority of these methods rely on the assumption that the seismic load is introduced on the tunnel in a quasi-static manner, and therefore they do not account for the dynamic soil–structure interaction effects (Pitilakis & Tsinidis, 2014). In this section two of the most commonly used methods are discussed,

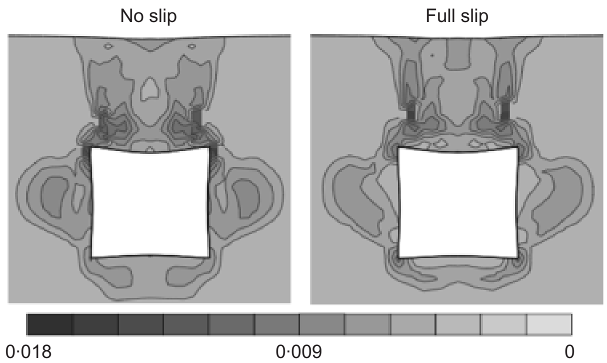

Fig. 14. Soil plastic deformations computed by the visco-elasto-plastic numerical analyses around tunnel at end of first flight (deformations scale ×10)

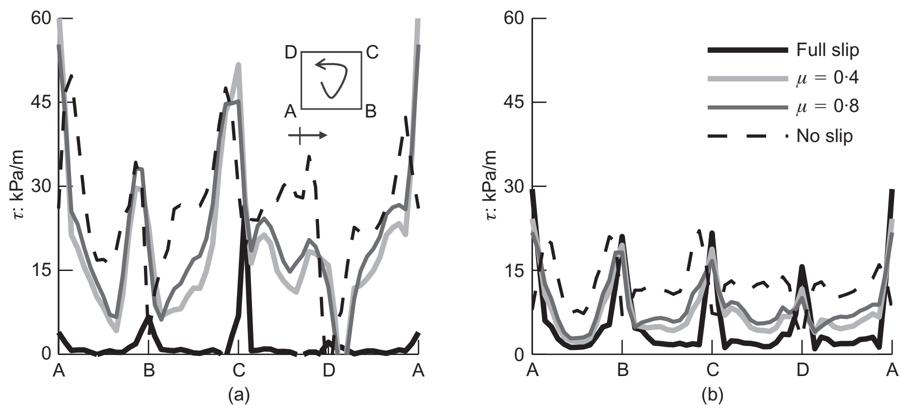

Fig. 15. Effect of the soil–tunnel interface properties on the soil dynamic shear stress distributions computed along the perimeter of the tunnel at the time step of maximum racking distortion: (a) earthquake EQ4; (b) earthquake EQ7

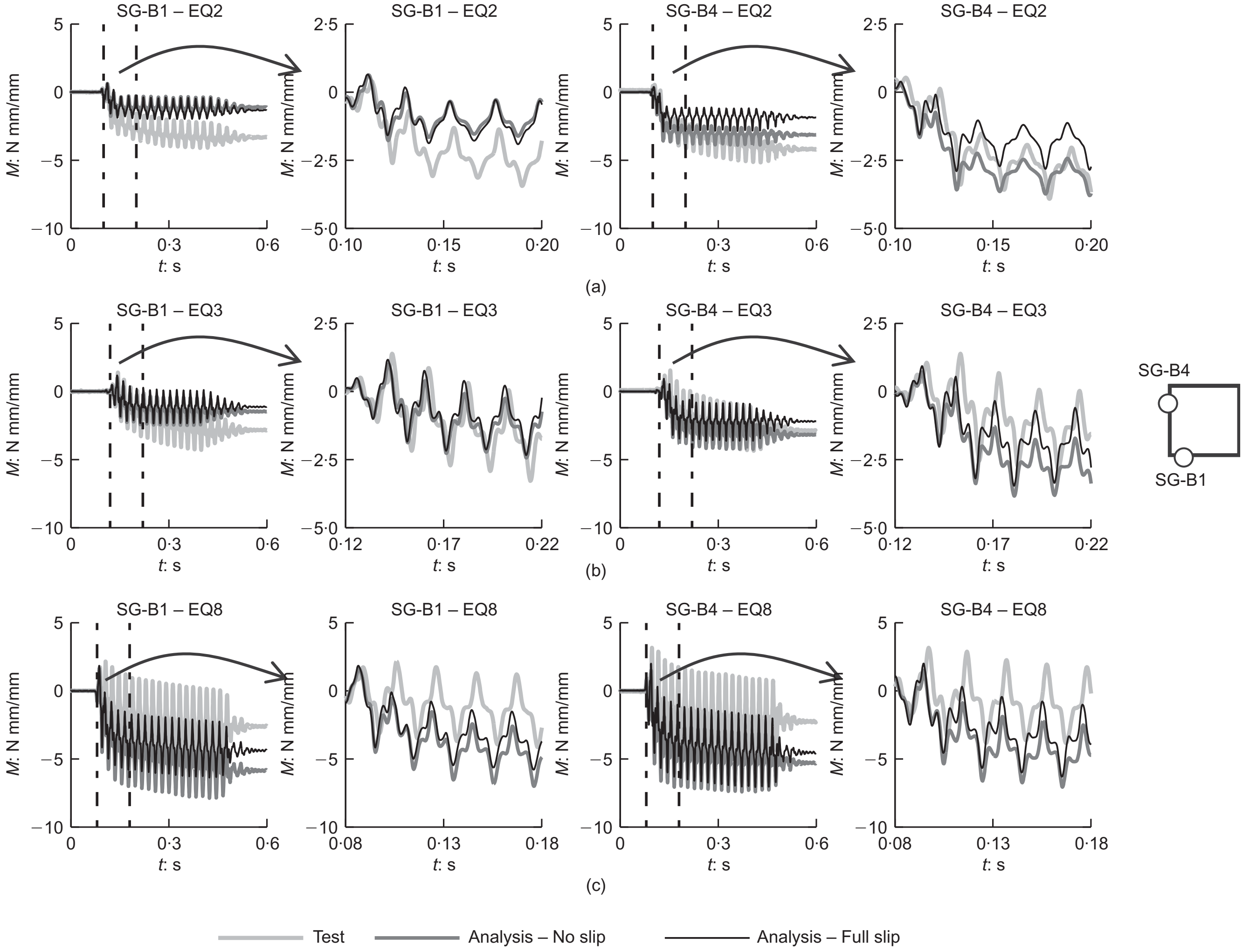

Fig. 16. Dynamic bending moment–time histories recorded and computed by visco-elasto-plastic analysis for different earthquake input motions, effect of the soil–tunnel interface properties: (a) earthquake EQ2; (b) earthquake EQ3; (c) earthquake EQ8

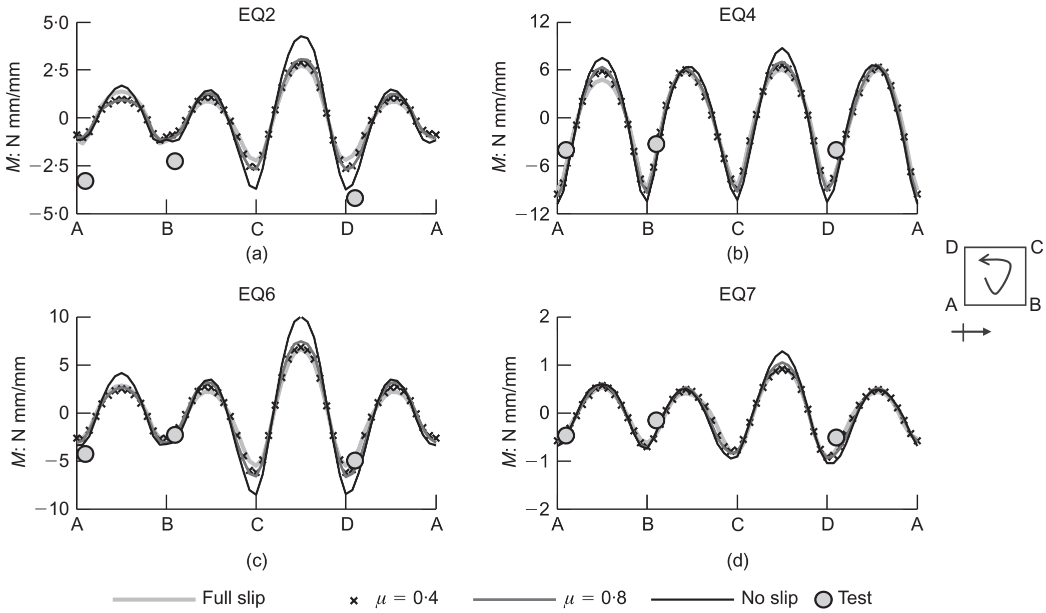

Fig. 17. Residual dynamic bending moment distributions along the perimeter of the tunnel, recorded and computed by visco-elasto-plastic analyses at the end of shaking: (a) earthquake EQ2; (b) earthquake EQ4; (c) earthquake EQ6; (d) earthquake EQ7

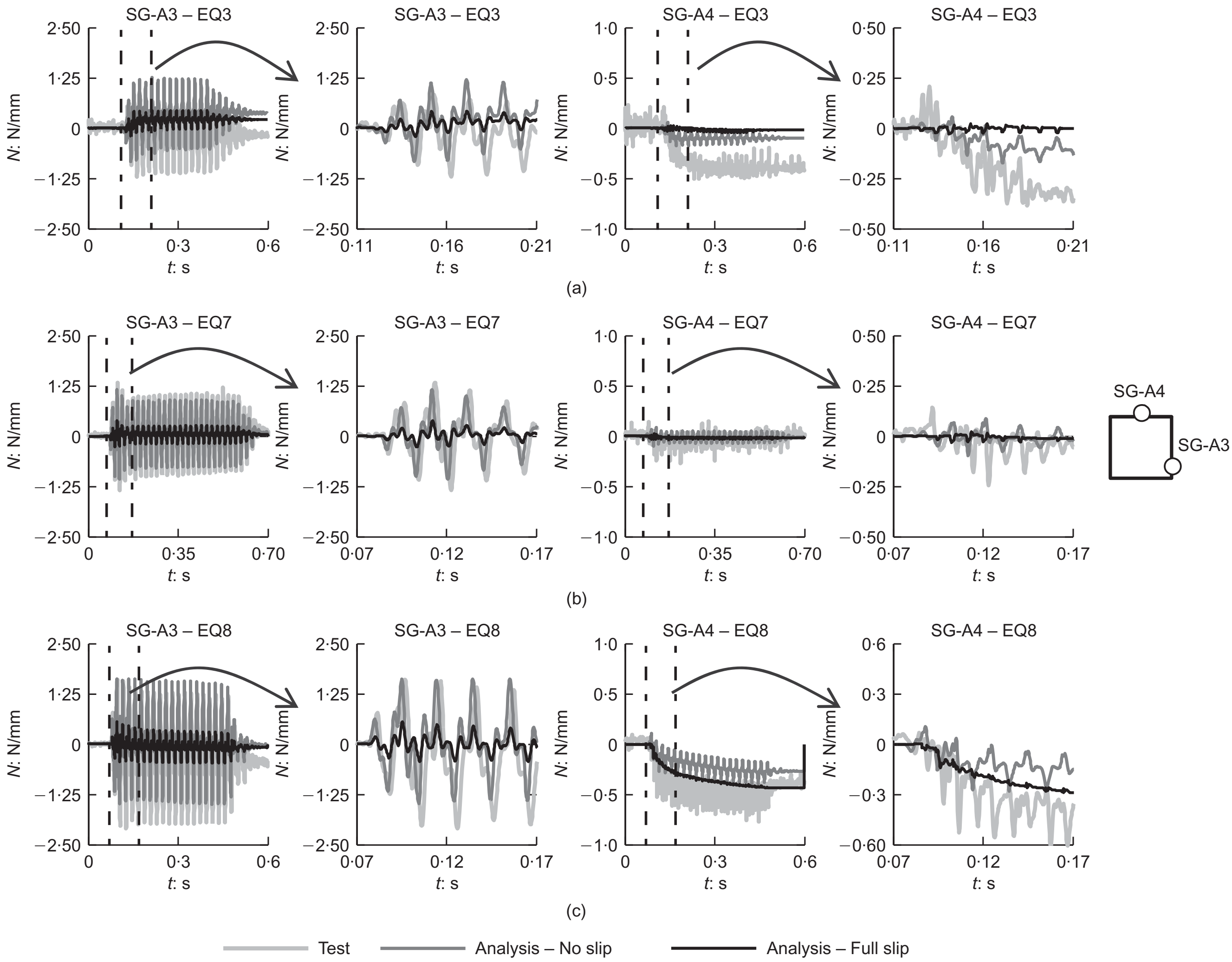

Fig. 18. Dynamic axial force–time histories recorded and computed by visco-elasto-plastic analysis for different earthquake input motions, effect of the soil–tunnel interface properties: (a) earthquake EQ3; (b) earthquake EQ7; (c) earthquake EQ8

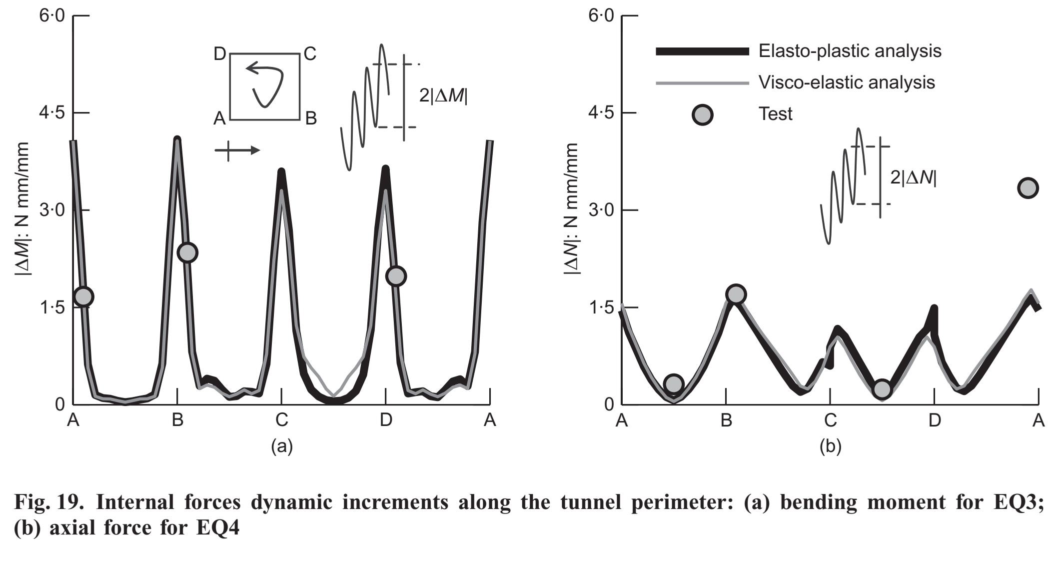

Fig. 19. Internal forces dynamic increments along the tunnel perimeter: (a) bending moment for EQ3; (b) axial force for EQ4

namely, the design procedure proposed by Wang (1993) and the pseudo-static seismic coefficient deformation method (FHWA, 2009) or detailed equivalent static analysis method (ISO, 2005).

According to the first methodology, the tunnel seismic response is evaluated through a simple static frame analysis. The structural racking distortion due to ground shaking is modelled as an equivalent static load or pressure that is imposed on the frame (Fig. 20(a)). This 'structural' racking distortion is evaluated by the free-field ground racking distortion, which is properly adjusted, through the so-called racking ratio (structural to ground racking distortions), in order to account for the soil–tunnel interaction effects. The racking ratio is correlated with relative flexibility of the soil

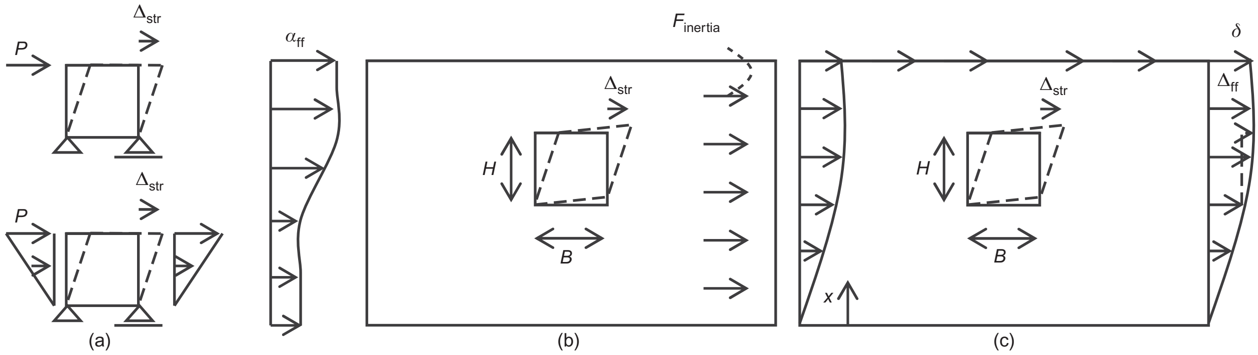

Fig. 20. Schematic representation of the simplified analysis methods: (a) Wang (1993) simplified method, (b) detailed equivalent static analysis method, distributed inertial loads, (c) detailed equivalent static analysis method, imposed deformations at model boundaries

to the tunnel that is expressed through the flexibility ratio F (Wang, 1993)

$$F = \frac{G \times B}{S \times H} \tag{3}$$

where G is the soil shear modulus, B and H are the width and the height of the structure, respectively, and S is the required force to cause a unit racking deflection of the structure.

According to NCHPR611 regulations (Anderson *et al.*, 2008) the racking ratio can be computed as

$$R = \frac{\Delta_{str}}{\Delta_{ff}} = \frac{2F}{(1+F)} \tag{4}$$

In the detailed equivalent static analysis method, a 2D soil–tunnel numerical model is proposed for the analysis, similar to the dynamic analysis (ISO, 2005; FHWA, 2009). The seismic load is introduced in a pseudo-static manner, as equivalent inertial load throughout the entire model that corresponds to the ground free-field acceleration amplification profile (Fig. 20(b)). In an alternative to this method, equivalent seismic load is introduced as a ground deformation pattern on the numerical model boundaries (Fig. 20(c)), corresponding to the free-field ground response (Kontoe *et al.*, 2008; Hashash *et al.*, 2010).

The test case presented herein is used as a case study to verify the effectiveness of the aforementioned simplified methods. More specifically, the results of the implemented simplified methods are compared to the calibrated dynamic analysis that is used as the benchmark case. The comparisons are made in terms of computed racking ratio and dynamic bending moment in the lining, which are considered to be representative parameters for the validation. The flexibility ratio for the given case is estimated equal to $F = 62{\cdot}5$, indicating a quite flexible structure compared to the surrounding soil. To further extend the comparisons, a second series of analyses are performed, increasing the tunnel lining thickness, in order to model a rigid tunnel ($F = 0{\cdot}29$). Both static and dynamic analyses are performed separately for each earthquake scenario, using the numerical model presented in Fig. 4. Although simplified methods propose an equivalent linear approximation (e.g. degraded shear modulus computed from site response analysis) to account for the soil non-linear response under ground shaking (e.g. FHWA, 2009), both elastic and elasto-plastic analyses are performed, using the constitutive models presented before, in order to check the effect of the soil yielding response on the results. Moreover, to study the effect of the soil–tunnel interface properties, the analyses are carried out under full slip and no-slip conditions. Sand mechanical properties (e.g. stiffness and strength) are selected in order to correspond with those of the dynamic analysis, while the equivalent seismic loads (e.g. inertia forces or ground displacements) are computed from the dynamic analysis, referring to the free field and for the time step of maximum tunnel racking distortion. To investigate the effect of the input motion amplitude, the analyses are performed for EQ3 ($0{\cdot}13\boldsymbol{g}$) and for EQ4 ($0{\cdot}24\boldsymbol{g}$) according to Table 4, whereas to study the input motion frequency content on the response, a final set of analyses is performed using the Japanese Meteorological Agency (JMA) record from the 1995 Kobe earthquake scaled down to $0{\cdot}24\boldsymbol{g}$. The following presented results refer to extreme scenarios regarding the tunnel flexibility and therefore they should be interpreted as limit cases. Soil strength parameters may affect the soil yielding response and therefore may alter the results of non-linear analyses. Considering the relatively low strength estimated in the examined cases and the associated increased yielding response, the results may be considered conservative.

Table 5 presents representative comparisons of racking ratios estimated from different approaches for EQ4, assuming elastic soil response. Generally, the numerical results for no-slip conditions resulted in larger racking ratios (12–35% larger) compared to the full slip conditions. Moreover, racking ratios computed from the equivalent static analyses seem to be slightly lower (15–20%) compared to the dynamic analysis results. The NCHPR611 analytical relation (Anderson *et al.*, 2008) overestimates the racking ratio for the flexible tunnel, while for the rigid tunnel, assuming no-slip

Table 5. Racking ratios estimated by different methods under the assumption of elastic soil response for EQ4

Case	Dynamic analysis	Equivalent static analysis – force	Equivalent static analysis – displacement	NCHPR611 Anderson *et al.* (2008) – ($R = 2F/(1+F)$)
Flexible tunnel – full slip	1·3	1·27	1·22	1·96
Flexible tunnel – no slip	1·46	1·42	1·40	1·96
Rigid tunnel – full slip	0·5	0·47	0·40	0·45
Rigid tunnel – no slip	0·74	0·72	0·65	0·45

conditions, numerical analyses result in a ratio larger than the analytical estimation. An underestimation of the racking ratio will result in underestimation of the lining forces (e.g. implementing Wang's method). On the contrary, an overestimation of the racking ratio may lead to an overdesign that may be considered as a conservative 'safe' design concept. However, overdesign is not only needlessly expensive but may lead to the stiffening of the structure, which may in turn change the whole response pattern in a detrimental way.

Figure 21 presents representative comparisons of the dynamic bending moment distributions along the tunnel's perimeter, computed with different design methods, assuming no-slip conditions. The elasto-plastic analyses numerical results for the flexible tunnel case are also compared with the experimental data (Fig. 21(b)). Table 6 tabulates similar comparisons between the recorded and the computed dynamic bending moment at the locations of the strain gauges. Numerical results correspond to full-slip conditions in this case. Generally, for the assumption of elastic soil response, the equivalent static analyses reproduce well the computed bending moment distribution from the dynamic analysis. However, the maximum bending moment is underestimated for both the flexible and the rigid tunnel, especially when the equivalent seismic load is introduced in terms of deformation at the model boundaries.

In the case of the elasto-plastic analyses, bending moment distributions are more complex, especially for the flexible tunnel, due to the associated larger soil yielding. Experimental data are generally closer to the dynamic analysis results (Fig. 21(b) and Table 6). Actually, equivalent static analyses results barely follow the experimental data and the bending moment distribution computed by the dynamic analysis, exhibiting values which are considerably lower. For the rigid tunnel case, simplified analyses results are closer to the dynamic analysis, but again the differences are quite noticeable. It is obvious that simplified methods cannot reproduce the soil loading history during shaking as efficiently as the dynamic analysis. This loading history affects significantly the soil permanent response. Similar to the elastic analyses, the differences are higher for the cases where the equivalent seismic loads are introduced in terms of imposed ground displacement at the boundaries. Local yielding at these boundary locations may affect the tunnel loading.

Table 6. Comparisons between recorded and computed – from different design methods – bending moments at receivers' positions (EQ3 elasto-plastic analyses for full slip conditions)

Position	*M*: N mm/mm			
	Full dynamic analysis	Equivalent static analysis – force	Equivalent static analysis – deformation	Test
SG-B1	−3·90	−2·55	−1·74	−4·16
SG-B2	−1·59	−0·25	−0·20	−3·59
SG-B4	−4·00	−1·10	−0·25	−4·21

Figure 22 plots static to dynamic bending moment ratios that are computed at a crucial lining section (joint C, Fig. 21) under different assumptions regarding the soil–tunnel interface properties, the soil response (elastic and elasto-plastic) and the input motion characteristics. Generally, equivalent static analyses underestimate the bending moment compared to the full dynamic analysis. For the elastic analyses, the differences may reach 20 to 40%. The discrepancies are even higher for the elasto-plastic analyses (differences up to 60%), especially for the flexible tunnel case. The differences are generally higher for the cases where the equivalent seismic load is introduced in terms of ground displacements at the model boundaries. This may be attributed to the relatively large distance between the tunnel and the numerical model boundaries (14·3 m for the side boundaries), where the ground deformation is imposed. By increasing this distance it is possible that a greater amount of induced ground strain is artificially absorbed by the soil elements, thus 'relieving' the structure and altering the

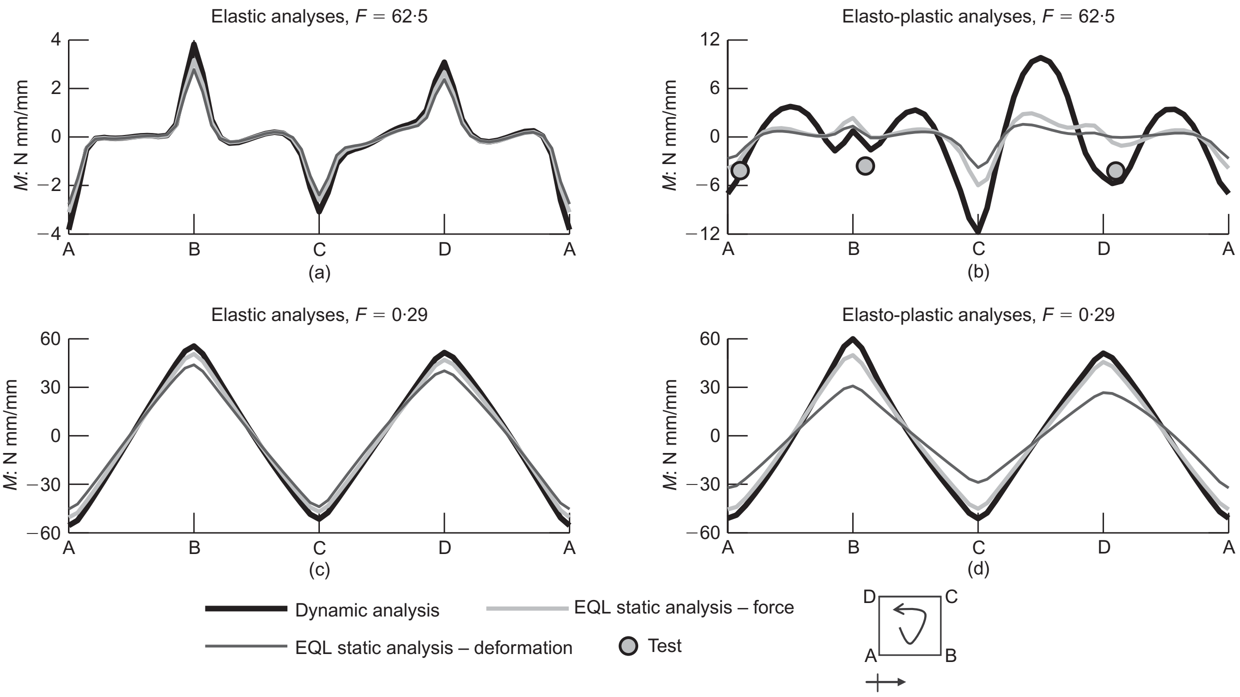

Fig. 21. Dynamic bending moment distributions along the tunnel perimeter computed from different methods for EQ3: (a) flexible tunnel–elastic analysis; (b) flexible tunnel–elasto-plastic analysis; (c) rigid tunnel–elastic analysis; (d) rigid tunnel–elasto-plastic analysis

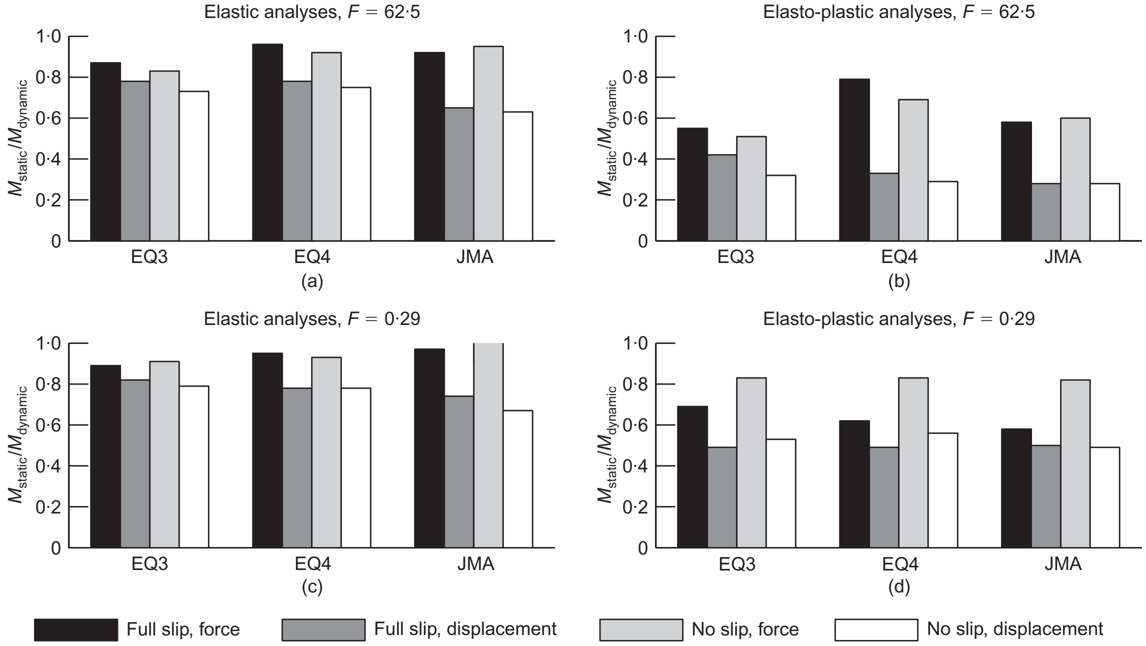

Fig. 22. Static to dynamic bending moment ratios computed at the right side-wall–roof slab corner: (a) flexible tunnel–elastic analysis; (b) flexible tunnel–elasto-plastic analysis; (c) rigid tunnel–elastic analysis; (d) rigid tunnel–elasto-plastic analysis

analysis results (Pitilakis & Tsinidis, 2014). It is worth noting that Hashash *et al.* (2010) propose this distance to be significantly smaller. Soil–tunnel interface properties and input motion characteristics seem to have a minor effect on the computed ratios in case of the elastic analyses, whereas these parameters become more important in the case of the elasto-plastic analyses (especially in the case of the flexible tunnel), owing to their effect on the soil yielding response.

CONCLUSIONS

The paper presented representative experimental results from a series of dynamic centrifuge tests on a flexible model tunnel embedded in dry sand, along with results from numerical simulations of the tests. Numerical models were found capable of reproducing the recorded response with reasonable engineering accuracy. Some inevitable differences between the recorded and the computed response are attributed to the difficulties in ascertaining precisely the soil, tunnel and soil–tunnel interface mechanical properties of the centrifuge model. To a certain degree this also depends on the constitutive models used; however, these models are adequately calibrated. All constitutive models actually constitute an approximation of the actual sand behaviour under seismic loading. Their accuracy depends on numerous parameters, which are mainly affected by the typology and the complexity of the problem modelled. Sometimes modelling very complex problems, such as the one in this paper, using complicated constitutive models for the soil, which could not be well calibrated, may increase considerably the uncertainties and reduce the accuracy of the results. The use of the models implemented herein and the comparisons to the experimental data are an additional verification of their efficiency to model complicated problems such as the one presented in this paper.

With regard to the tunnel's response: both the experimental and the numerical data revealed a rocking mode of vibration for the tunnel in addition to the racking distortion. Inward deformations were also observed due to the high flexibility of the tunnel. Post-earthquake residual values were recorded experimentally and predicted numerically for the earth pressures on the side walls and the lining forces, which were amplified by the increased flexibility of the tunnel. This complex response associated with residual deformations and internal forces in the lining cannot be reproduced by the equivalent linear approximation method that is often proposed in regulations and used in engineering practice. Therefore, this approach should be used with caution, especially when the tunnel is quite flexible and high soil non-linearity is expected, as in the case of strong earthquakes.

The calibrated dynamic numerical models were finally used as a benchmark to validate the accuracy of currently used simplified methods. Racking ratios computed from the equivalent static analyses were found to be slightly lower compared to the dynamic analysis results, while the NCHPR611 analytical relation (Anderson *et al.*, 2008) was found to overestimate the racking ratio for the flexible tunnel case. In general, simplified methods underestimated the tunnel lining forces compared to the full dynamic analysis. Assuming an elastic soil response, the differences were up to 30%, and the discrepancies were much higher for the cases when the soil permanent deformation was accounted for. Equivalent static analyses, where the load is introduced in terms of distributed inertial loads throughout the model, were found to be more efficient. The main conclusion drawn is that simplified methods should be used with caution, mainly during preliminary stages of design, and for cases where high soil non-linearity is not expected (e.g. rather low to medium seismic intensities).

ACKNOWLEDGEMENTS

The research leading to the presented experimental results has received funding from the European Community's Seventh Framework Programme (FP7/2007–2013) for access to the Turner beam centrifuge, Cambridge, UK, under grant agreement no. 227887 (SERIES – Seismic Engineering Research Infrastructures for European Synergies, http://www.series.upatras.gr/). The excellent technical support received by the technicians at the Schofield Centre is gratefully acknowledged.

NOTATION

A	acceleration amplitude
a	input motion amplitude
a_{ff}	soil free-field horizontal acceleration
B	tunnel width
c	cohesion
D	damping of sand
d_{10}	sand grain diameter at 10% passing
d_{50}	sand grain diameter at 50% passing
d_{60}	sand grain diameter at 60% passing
E	aluminium alloy Young's modulus
E_{c}	concrete Young's modulus
e	sand void ratio
$e_{\max}$	maximum sand void ratio
$e_{\min}$	minimum sand void ratio
F	soil to tunnel flexibility ratio
F_{inertia}	equivalent to acceleration inertial load
f	input motion dominant frequency
f_{bk}	aluminium alloy tensile strength
G	sand reduced shear modulus
$G_{\max}$	sand small-strain shear modulus
H	tunnel height
K_0	earth coefficient at rest
l	length
M	lining bending moment per unit length
M_{dynamic}	lining bending moment evaluated through dynamic analysis
M_{static}	lining bending moment evaluated through equivalent static analysis
m	mass
N	lining axial load per unit length
n	scale factor
P	equivalent to tunnel racking distortion force
R	racking ratio
RC	resonant column tests
S	required force to cause a unit racking deflection of the tunnel
t	time
TX	cyclical triaxial tests
V_{so}	small-strain shear velocity gradient of sand
α	reduction coefficient for sand shear modulus during shaking
γ	shear strain
γ_{t}	aluminium alloy unit weight
Δ_{ff}	free-field ground racking distortion
Δ_{str}	tunnel racking distortion
$\lvert\Delta M\rvert$	lining bending moment dynamic increment
$\lvert\Delta N\rvert$	lining axial force dynamic increment
δ	horizontal deformation at soil surface
μ	soil–tunnel interface friction coefficient
ν	aluminium alloy Poisson ratio
ρ_{s}	sand density
σ	dynamic earth pressure per unit length
σ'	mean effective stress
τ	dynamic shear stress per unit length
ϕ	sand friction angle
ϕ_{cv}	sand critical friction angle
ψ	sand dilatancy angle

REFERENCES

Abaqus (2012). *Abaqus: theory and analysis user's manual version 6.12*. Providence, RI, USA: Dassault Systèmes Simulia.

AFPS/AFTES (2001). *Guidelines on earthquake design and protection of underground structures*, Version 1. Paris, France: Working Group of the French Association for Seismic Engineering (AFPS) and French Tunnelling Association (AFTES).

Amorosi, A. & Boldini, D. (2009). Numerical modelling of the transverse dynamic behaviour of circular tunnels in clayey soils. *Soil Dynam. Earthquake Engng* **29**, No. 6, 1059–1072, http://dx.doi.org/10.1007/s11440-013-0295-7.

Amorosi, A., Boldini, D. & Falcone, G. (2014). Numerical prediction of tunnel performance during centrifuge dynamic tests. *Acta Geotechnica* **9**, No. 4, 581–596, http://dx.doi.org/10.1007/s11440-013-0295-7.

Anastasopoulos, I. & Gazetas, G. (2010). Analysis of cut-and-cover tunnels against large tectonic deformation. *Bull. Earthquake Engng* **8**, No. 2, 283–307, http://dx.doi.org/10.1007/s10518-009-9135-4.

Anastasopoulos, I., Gerolymos, N., Drosos, V., Kourkoulis, R. & Georgarakos, T. (2007). Nonlinear response of deep immersed tunnel to strong seismic shaking. *J. Geotech. Geoenviron. Engng* **133**, No. 9, 1067–1090, http://dx.doi.org/10.1061/(ASCE)1090-0241(2007)133:9(1067).

Anastasopoulos, I., Gerolymos, N., Drosos, V., Georgarakos, T., Kourkoulis, R. & Gazetas, G. (2008). Behaviour of deep immersed tunnel under combined normal fault rupture deformation and subsequent seismic shaking. *Bull. Earthquake Engng* **6**, No. 2, 213–239, http://dx.doi.org/10.1007/s10518-007-9055-0.

Anderson, D. G., Martin, G. R., Lam, I. & Wang, J. N. (2008). *NCHPR611: Seismic analysis and design of retaining walls, buried structures, slopes and embankments*. Washington, DC, USA: National Cooperative Highway Research Program, Transportation Research Board.

Bardet, J. B., Ichii, K. & Lin, CH. (2000). *EERA: a computer program for equivalent-linear earthquake site response analyses of layered soil deposits*. Los Angeles, CA, USA: University of Southern California, Department of Civil Engineering.

Bilotta, E., Lanzano, G., Madabhushi, S. P. G. & Silvestri, F. (2014). A numerical round robin on tunnels under seismic actions. *Acta Geotechnica* **9**, No. 4, 563–579, http://dx.doi.org/10.1007/s11440-014-0330-3.

Bobet, A. (2010). Drained and undrained response of deep tunnels subjected to far-field shear loading. *Tunnell. Underground Space Technol*. **25**, No. 1, 21–31, http://dx.doi.org/10.1016/j.tust.2009.08.001.

Bobet, A., Fernandez, G., Huo, H. & Ramirez, J. (2008). A practical iterative procedure to estimate seismic-induced deformations of shallow rectangular structures. *Can. Geotech. J.* **45**, No. 7, 923–938, http://dx.doi.org/10.1139/T08-026.

Brennan, A. J., Thusyanthan, N. I. & Madabhushi, S. P. G. (2005). Evaluation of shear modulus and damping in dynamic centrifuge tests. *J. Geotech. Geoenviron. Engng* **131**, No. 12, 1488–1497, http://dx.doi.org/10.1061/(ASCE)1090-0241(2005)131:12(1488).

Chen, G., Wang, Z., Zuo, X., Du, X. & Gao, H. (2013). Shaking table test on seismic failure characteristics of a subway station structure in liquefiable ground. *Earthquake Engng Structl Dynam.* **42**, No. 10, 1489–1507, http://dx.doi.org/10.1002/eqe.2283.

Chian, S. C. & Madabhushi, S. P. G. (2012). Effect of buried depth and diameter on uplift of underground structures in liquefied soils. *Soil Dynam. Earthquake Engng* **41**, No. 1, 181–190, http://dx.doi.org/10.1016/j.soildyn.2012.05.020.

Chou, J. C., Kutter, B. L., Travasarou, T. & Chacko, J. M. (2010). Centrifuge modelling of seismically induced uplift for the BART transbay tube. *J. Geotech. Geoenviron. Engng* **137**, No. 8, 754–765, http://dx.doi.org/10.1061/(ASCE)GT.1943–5606.0000489.

Cilingir, U. (2009). *Seismic response of tunnels*. PhD thesis, University of Cambridge, UK.

Cilingir, U. & Madabhushi, S. P. G. (2011a). A model study on the effects of input motion on the seismic behaviour of tunnels. *Soil Dynam. Earthquake Engng* **31**, No. 3, 452–462, http://dx.doi.org/10.1016/j.soildyn.2010.10.004.

Cilingir, U. & Madabhushi, S. P. G. (2011b). Effect of depth on the seismic response of square tunnels. *Soils Found*. **51**, No. 3, 449–457, http://dx.doi.org/10.3208/sandf.51.449.

Cilingir, U. & Madabhushi, S. P. G. (2011c). Effect of depth on the seismic response of circular tunnels. *Can. Geotech. J.* **48**, No. 1, 117–127, http://dx.doi.org/10.1139/T10-047.

Conti, R., Viggiani, G. M. B. & Perugini, F. (2014). Numerical modelling of centrifuge dynamic tests of circular tunnels in dry sand. *Acta Geotechnica* **9**, No. 4, 597–612, http://dx.doi.org/10.1007/s11440-13-0286-8.

Dowding, C. H. & Rozen, A. (1978). Damage to rock tunnels from earthquake shaking. *J. Geotech. Engng Div., ASCE* **104**, No. 2, 175–191.

FHWA (Federal Highway Administration) (2009). *Technical manual for design and construction of road tunnels – Civil elements*, Publication No. FHWA-NHI-10-034. Washington, DC, USA: U. S. Department of Transportation, Federal Highway Administration.

Ghosh, B. & Madabhushi, S.P.G. (2002). An efficient tool for measuring shear wave velocity in the centrifuge. In *Proceedings of international conference on physical modelling in geotechnics* (eds R. Phillips, P. J. Guo and R. Popescu), pp. 119–124. St Johns, NF, Canada: Balkema.

Gomes, R. C. (2014). Numerical simulation of the seismic response of tunnels in sand with an elastoplastic model. *Acta Geotechnica* **9**, No. 4, 613–629, http://dx.doi.org/10.1007/s11440-013-0287-7.

Hardin, B. O. & Drnevich, V. P. (1972). Shear modulus and damping in soils. *J. Soil Mech. Found. Div., ASCE* **98**, No. 7, 667–692.

Hashash, Y. M. A., Hook, J. J., Schmidt, B. & Yao, J. I.-C. (2001). Seismic design and analysis of underground structures. *Tunnell. Underground Space Technol*. **16**, No. 2, 247–293, http://dx.doi.org/10.1016/S0886-7798(01)00051-7.

Hashash, Y. M. A., Park, D. & Yao, J. I. C. (2005). Ovaling deformations of circular tunnels under seismic loading, an update on seismic design and analysis of underground structures. *Tunnell. Underground Space Technol*. **20**, No. 5, 435–441, http://dx.doi.org/10.1016/j.tust.2005.02.004.

Hashash, Y. M. A., Karina, K., Koutsoftas, D. & O'Riordan, N. (2010). Seismic design considerations for underground box structures. In *Proceedings of the earth retention conference 3* (eds R. Finno, Y. M. A. Hashash and P. Arduino), pp. 620–637, http://dx.doi.org/10.1061/41128(384)64. Bellevue, WA, USA: ASCE.

Hleibieh, J., Wagener, D. & Herle, I. (2014). Numerical simulation of a tunnel surrounded by sand under earthquake using a hypoplastic model. *Acta Geotechnica* **9**, No. 4, 631–640, http://dx.doi.org/10.1007/s11440-013-0294-8.

Huo, H., Bodet, A., Fernández, G. & Ramirez, J. (2005). Load transfer mechanisms between underground structure and surrounding ground: evaluation of the failure of the Daikai station. *J. Geotech. Geoenviron. Engng* **131**, No. 12, 1522–1533, http://dx.doi.org/10.1061/(ASCE)1090-0241(2005)131:12(1522).

Huo, H., Bodet, A., Fernandez, G. & Ramirez, J. (2006). Analytical solution for deep rectangular structures subjected to far-field shear stresses. *Tunnell. Underground Space Technol*. **21**, No. 6, 613–625, http://dx.doi.org/10.1016/j.tust.2005.12.135.

Hwang, J.-H. & Lu, C.-C. (2007). Seismic capacity assessment of old Sanyi railway tunnels. *Tunnell. Underground Space Technol*. **22**, No. 4, 433–449, http://dx.doi.org/10.1016/j.tust.2006.09.002.

Iida, H., Hiroto, T., Yoshida, N. & Iwafuji, M. (1996). Damage to Daikai subway station Japanese Geotechnical Society, Japan. *Soils Found.*, Special Issue on Geotechnical Aspects of the January 17 1995, Hyogoken-Nambu Earthquake, 283–300.

Ishibashi, I. & Zhang, X. (1993). Unified dynamic shear moduli and damping ratios of sand and clay. *Soils Found*. **33**, No. 1, 182–191.

ISO (International Organization for Standardization) (2005). ISO 23469: Bases for design of structures – Seismic actions for designing geotechnical works, International Standard ISO TC 98/SC3/WG10. Geneva, Switzerland: International Organization for Standardization.

Jaky, J. (1948). The coefficient of earth pressure at rest. *J. Union Hungarian Engrs Architects* **78**, No. 22, 355–358.

Kawashima, K. (2000). Seismic design of underground structures in soft ground: a review. In *Geotechnical aspects of underground construction in soft ground* (eds O. Kusakabe, K. Fujita and Y. Miyazaki). Rotterdam, the Netherlands: Balkema.

Kirtas, E., Rovithis, E. & Pitilakis, K. (2009). Subsoil interventions effect on structural seismic response. Part i: validation of numerical simulations. *J. Earthquake Engng* **13**, No. 2, 155–169, http://dx.doi.org/10.1080/13632460802347463.

Kontoe, S., Zdravkovic, L., Potts, D. & Mentiki, C. (2008). Case study on seismic tunnel response. *Can. Geotech. J.* **45**, No. 12, 1743–1764, http://dx.doi.org/10.1139/T08-087.

Kontoe, S., Zdravkovic, L., Potts, D. & Mentiki, C. (2011). On the relative merits of simple and advanced constitutive models in dynamic analysis of tunnels. *Géotechnique* **61**, No. 10, 815–829, http://dx.doi.org/10.1680/geot.9.P.141.

Kontoe, S., Avgerinos, V. & Potts, D. M. (2014). Numerical validation of analytical solutions and their use for equivalent-linear seismic analysis of circular tunnels. *Soil Dynam. Earthquake Engng* **66**, No. 1, 206–219, http://dx.doi.org/10.1016/j.soildyn.2014.07.004.

Lanzano, G., Bilotta, E., Russo, G., Silvestri, F. & Madabhushi, S. P. G. (2010). Dynamic centrifuge tests on shallow tunnel models in dry sand. *Proceedings of the VII international conference on physical modelling in geotechnics (ICPMG 2010)*, pp. 561–567. Zurich, Switzerland: Taylor and Francis.

Lanzano, G., Bilotta, E., Russo, G., Silvestri, F. & Madabhushi, S. P. G. (2012). Centrifuge modelling of seismic loading on tunnels in sand. *Geotech. Testing J.* **35**, No. 6, 10–26, http://dx.doi.org/10.1520/GTJ104348.

Lanzano, G., Bilotta, E., Russo, G. & Silvestri, F. (2014). Experimental and numerical study on circular tunnels under seismic loading. *Eur. J. Environ. Civ. Engng*, http://dx.doi.org/10.1080/19648189.2014.893211.

Li, Z., Escoffier, S. & Kotronis, P. (2013). Using centrifuge tests data to identify the dynamic soil properties: Application to Fontainebleau sand. *Soil Dynam. Earthquake Engng* **52**, No. 1, 77–87, http://dx.doi.org/10.1016/j.soildyn.2013.05.004.

Madabhushi, S. P. G., Schofield, A. N. & Lesley, S. (1998). A new stored angular momentum (SAM) based actuator. In *Proceedings of the international conference, centrifuge 98* (eds T. Kimura, O. Kusakabe and J. Takemura), pp. 111–116. Tokyo, Japan: Balkema.

Madabhushi, S. P. G., Houghton, N. E. & Haigh, S. K. (2006). A new automatic sand pourer for model preparation at University of Cambridge. In *Physical modelling in geotechnics – 6th ICPMG 08* (eds C. W. W. Ng, L. M. Zhang and Y. H. Wang), pp. 217–222. London, UK: Taylor and Francis.

Pakbaz, M. & Yareevand, A. (2005). 2-D analysis of circular tunnel against earthquake loading. *Tunnell. Underground Space Technol*. **20**, No. 5, 411–417, http://dx.doi.org/10.1016/j.tust.2005.01.006.

Penzien, J. (2000). Seismically induced racking of tunnel linings. *Earthquake Engng Structl Dynamics* **29**, No. 5, 683–691.

Pistolas, G. A., Tsinaris, A., Anastasiadis, A. & Pitilakis, K. (2014). Undrained dynamic properties of Hostun sand. *Proceedings of 7th Greek geotechnics conference*, Athens, Greece. Athens, Greece: Hellenic Society of Soil Mechanics and Geotechnical Engineering (in Greek).

Pitilakis, D. & Clouteau, D. (2010). Equivalent linear substructure approximation of soil–foundation–structure interaction: model presentation and validation. *Bull. Earthquake Engng* **8**, No. 2, 257–282, http://dx.doi.org/10.1007/s10518-009-9128-3.

Pitilakis, K. & Tsinidis, G. (2014). Performance and seismic design of underground structures. In *Earthquake geotechnical engineering design* (eds M. Maugeri and C. Soccodato), Geotechnical Geological and Earthquake Engineering, vol. 28, pp. 279–340, http://dx.doi.org/10.1007/978-3-319-03182-8_11. Geneva, Switzerland: Springer.

Schanz, T. & Vermeer, P. A. (1996). Angles of friction and dilatancy of sand. *Géotechnique* **46**, No. 1, 145–151, http://dx.doi.org/10.1680/geot.1996.46.1.145.

Schofield, A. N. (1980). Cambridge geotechnical centrifuge operations. *Géotechnique* **30**, No. 3, 227–268, http://dx.doi.org/10.1680/geot.1980.30.3.227.

Schofield, A. N. (1981). Dynamic and earthquake centrifuge modelling. *Proceedings of international conference on advances in geotechnical earthquake engineering and soil dynamics*, pp. 1081–1100. Rolla, MO, USA: University of Missouri.

Seed, H. B., Wong, R. T., Idriss, I. M. & Tokimatsu, K. (1986). Moduli and damping factors for dynamic analyses of cohesionless soils. *J. Geotech. Engng* **112**, No. 11, 1016–1032, http://dx.doi.org/10.1061/(ASCE)0733-9410(1986)112:11(1016).

Sharma, S. & Judd, W. R. (1991). Underground opening damage from earthquakes. *Engng Geol*. **30**, No. 3–4, 263–276, http://dx.doi.org/10.1016/0013-7952(91)90063-Q.

Shibayama, S., Izawa, J., Takahashi, A., Takemura, J. & Kusakabe, O. (2010). Observed behavior of a tunnel in sand subjected to shear deformation in a centrifuge. *Soils Found*. **50**, No. 2, 281–294, http://dx.doi.org/10.3208/sandf.50.281.

St John, C. M. & Zahrah, TF. (1987). Aseismic design of underground structures. *Tunnell. Underground Space Technol*. **2**, No. 2, 165–197, http://dx.doi.org/10.1016/0886-7798(87)90011-3.

Tsinidis, G., Heron, C., Pitilakis, K. & Madabhushi, S. P. G. (2014a). Physical modelling for the evaluation of the seismic behavior of square tunnels. In *Seismic evaluation and rehabilitation of structures* (eds A. Ilki and M. Fardis), Geotechnical Geological and

Earthquake Engineering, vol. 26, pp. 389–406, http://dx.doi.org/10.1007/978-3-319-00458-7_22. Geneva, Switzerland: Springer.

Tsinidis, G., Pitilakis, K. & Trikalioti, A. D. (2014b). Numerical simulation of round robin numerical test on tunnels using a simplified kinematic hardening model. *Acta Geotechnica* **9**, No. 4, 641–659, http://dx.doi.org/10.1007/s11440-013-0293-9.

Wang, J. N. (1993). *Seismic design of tunnels: A simple state of the art design approach*. New York, NY, USA: Parsons Brinckerhoff.

Wang, W. L., Wang, T. T., Su, J. J., Lin, C. H., Seng, C. R. & Huang, T. H. (2001). Assessment of damage in mountain tunnels due to the Taiwan Chi-Chi earthquake. *Tunnell. Underground Space Technol*. **16**, No. 3, 133–150, http://dx.doi.org/10.1016/S0886-7798(01)00047-5.

Zeghal, M. & Elgamal, A. W. (1994). Analysis of site liquefaction using earthquake records. *J. Geotech. Engng ASCE* **120**, No. 6, 996–1017, http://dx.doi.org/10.1061/(ASCE)0733-9410(1994)120:6(996).

Zeng, X. & Schofield, A. N. (1996). Design and performance of an equivalent shear beam (ESB) container for earthquake centrifuge modelling. *Géotechnique* **46**, No. 1, 83–102, http://dx.doi.org/10.1680/geot.1996.46.1.83.